

e^+ and \bar{p} production in pp collisions and the cosmic-ray e^+/\bar{p} flux ratio

Kfir Blum^{1,2}, Ryosuke Sato¹ and Masahiro Takimoto^{1,3}

¹*Department of Particle Physics and Astrophysics,*

Weizmann Institute of Science, Rehovot 7610001, Israel

²*CERN, Theoretical Physics Department, Geneva, Switzerland*

³*Institute of Particle and Nuclear Studies,*

High Energy Accelerator Research Organization (KEK),

Tsukuba 305-0801, Japan

(Dated: September 18, 2017)

Secondary astrophysical production of e^+ and \bar{p} cosmic rays is considered. Inclusive π , K , and \bar{p} production cross sections in pp collisions at large \sqrt{s} are parametrised using recent experimental data at LHC energies. The astrophysical production rate ratio $Q_{e^+}/Q_{\bar{p}}$ is calculated for an input cosmic ray proton flux consistent with local measurements. At $10 < E < 100$ GeV the cosmic ray flux ratio $J_{e^+}/J_{\bar{p}}$ measured by AMS02 falls below the production rate ratio by about 50%, while at high energy $E > 100$ GeV the measured flux ratio coincides with the production rate ratio of the secondary source.

I. INTRODUCTION

Cosmic ray (CR) antimatter is a potential probe of exotic high energy astrophysical phenomena and a unique diagnostic of CR propagation. Over the last decade, precise measurements of the flux of CR e^+ and \bar{p} extending to ever higher energies were reported by the PAMELA and AMS02 experiments [1–3]. The interpretation of these measurements motivates refined theoretical consideration of astrophysical e^+ and \bar{p} , produced as secondaries in the collision of primary CRs, notably protons, with interstellar matter (ISM), notably hydrogen. Our goal in the current paper is to improve on previous calculations of the inclusive production cross section of secondaries in pp collisions using recent accelerator data.

The main effect we wish to capture is the violation of radial scaling at $\sqrt{s} > 50$ GeV. As shown in Refs. [4–6], this effect leads to about a factor of two increase in the astrophysical \bar{p} source at \bar{p} energy above a few TeV. Here we evaluate the analogous effect in the CR e^+ source by analysing meson production at LHC energies. Earlier e^+ calculations were either based on too low \sqrt{s} data to see the effect [7–9] or relied on Monte-Carlo tools without direct verification in the kinematical regime relevant for astrophysics [10].

We aim to achieve $\sim 10\%$ accuracy for the astrophysical e^+ source at e^+ energy ranging from a few GeV up to multi-TeV; this accuracy goal is to be compared with the main radial scaling violation effect that is, again, about a factor of two at $E \sim 10$ TeV. As a check against earlier work, we also calculate the \bar{p} source to similar accuracy.

In section II we analyse the cross sections at large \sqrt{s} , using results from the NA49, PHENIX, ALICE, and CMS experiments. In section III we use these results to calculate the production rate ratio $Q_{e^+}/Q_{\bar{p}}$ for secondary e^+ and \bar{p} produced by a spectrum of high energy protons scattering on a proton target. We show that $Q_{e^+}/Q_{\bar{p}}$ is insensitive w.r.t. uncertainties in the primary proton

spectrum. At $10 < E < 100$ GeV the e^+/\bar{p} flux ratio measured by AMS02 falls below the production rate ratio by about 50%, while at high energy $E > 100$ GeV the measured flux ratio coincides with the production rate ratio of the secondary source. In App. A we discuss the contribution to secondary e^+ from K_L^0 decay, which was missing in previous calculations. In App. B we analyse the hyperon contribution to inclusive \bar{p} production. In App. C we reproduce the secondary cosmic ray \bar{p} flux predicted by using mean traversed target column density as deduced from cosmic ray nuclei data.

II. DATA ANALYSIS

Our baseline fitting formulae for inclusive hadron production in pp collisions are taken from Ref. [11] (Tan&Ng), which was based on $\sqrt{s} \leq 53$ GeV data and to which we provide corrections using the following new information:

- i. Tan&Ng’s formulae rely on radial scaling [12–14],

$$E \frac{d^3\sigma}{dp^3}(x_R, p_t, \sqrt{s}) \rightarrow_{\sqrt{s} \rightarrow \infty} E \frac{d^3\sigma}{dp^3}(x_R, p_t) \quad (1)$$

where $x_R = E^*/E_{\max}^*$, E^* is the final state hadron energy in the centre of mass (CM) frame and E_{\max}^* is the maximum attainable E^* . Recent accelerator data show violation of radial scaling in pp collisions at $\sqrt{s} \gtrsim 50$ GeV [15–19]. The $pp \rightarrow \bar{p}$ cross section increases at high energy [4–6] as compared to [11] and other early parametrisations. We will assess the analogous effect in meson production and the resulting e^+ yield.

- ii. In addition to the high energy end, unprecedented detailed measurements of the production cross section π^+ , K^\pm and \bar{p} [20–22] at $\sqrt{s} = 17.2$ GeV were reported by the NA49 experiment. This value of \sqrt{s} is particularly relevant for $E \sim 10 - 100$ GeV final state \bar{p} and e^+ [23]. We incorporate this data in our formulae for hadronic cross sections.

A. p_t -weighted cross sections and important kinematical region

Faced with an extensive data set [15–22], it is instructive to bracket the final state phase space that is most relevant for secondary CR production. In the fixed-target set up of high energy CR scattering on ambient ISM, the key quantity is the conversion cross section from incoming CR proton with ISM frame energy E_p to outgoing secondary particle with ISM frame energy E ,

$$\frac{d\sigma(E_p, E)}{dE} = 2\pi \int_0^\pi d\theta p_t \left(E \frac{d^3\sigma}{dp^3} \right) (x_R, p_t, \sqrt{s}), \quad (2)$$

where θ denotes the angle between the incoming proton and outgoing secondary in the ISM frame. The Lorentz-invariant differential cross section $E \frac{d^3\sigma}{dp^3}$ decreases sharply with increasing p_t , with the p_t -weighted cross section $p_t \left(E \frac{d^3\sigma}{dp^3} \right)$ peaking around average $\langle p_t \rangle \sim 0.2 - 0.4$ GeV. For $E \gg \langle p_t \rangle, m$, where m is the mass of the final state hadron of interest, we can simplify the integral as

$$\begin{aligned} & \int_0^\pi d\theta p_t \left(E \frac{d^3\sigma}{dp^3} \right) (x_R, p_t, \sqrt{s}) \\ & \simeq \frac{1}{p} \int_0^\infty dp_t p_t \left(E \frac{d^3\sigma}{dp^3} \right) (x_R|_{p_t=0}, p_t, \sqrt{s}), \end{aligned} \quad (3)$$

where $x_R|_{p_t=0}$ is computed at $p_t = 0$ and only depends on E and E_p . This exercise shows that, in the high energy regime, the p_t -weighted mean cross section with fixed x_R is the most important quantity for secondary CR production, allowing one to average over the detailed p_t dependence reported by the experiments.

Next, we consider the relevant range of x_R . Consider as a representative example the cross section parametrization [5]:

$$E \frac{d^3\sigma}{dp^3} (x_R, p_t) = f_0 e^{-\frac{p_t}{\langle p_t \rangle}} (1 - x_R)^n. \quad (4)$$

Typical parameters are $\langle p_t \rangle \simeq 0.2-0.4$ GeV and $n \simeq 5-7$. In the limit where $m^2/E^2, p_t^2/E^2 \ll 2m_p/E_p$, the astrophysical source term $Q(E)$ can be written as

$$\begin{aligned} Q(E) & \propto \int_E^\infty dE_p J_p(E_p) \frac{d\sigma(E_p, E)}{dE} \\ & \simeq 2\pi f_0 \langle p_t \rangle^2 J_p(E) \int_0^1 dx_R x_R^{\gamma-2} (1 - x_R)^n, \end{aligned} \quad (5)$$

where J_p denotes the CR proton flux and we assumed $J_p \propto E_p^{-\gamma}$. With $n \simeq 5-7$ and $\gamma \simeq 2.7$, the x_R integrand selects the range $\sim 0.1-0.4$.

To summarise, we are most interested in the cross section for secondary product energy in the range $E \gtrsim 10$ GeV. In this range, the relevant information is contained in the p_t -weighted mean invariant cross section at fixed x_R , where furthermore the relevant range of x_R is $\sim 0.1-0.4$.

B. Hadron production cross section

In this section we discuss the hadronic cross section in the light of recent collider experiments. We take the cross section fits by Tan&Ng as baseline, and derive corrections to these formula.

A comment is in order regarding the intermediate hyperon contribution to \bar{p} . In pp collisions, \bar{p} are generated promptly or by the decay of (relatively) long-lived hyperons, notably $\bar{\Lambda}$ and $\bar{\Sigma}^\pm$. The Tan&Ng \bar{p} fit includes the hyperon contributions. On the other hand, recent experiments such as NA49 report the prompt antiproton cross section in which the contribution of intermediate hyperon states is removed. Thus, when comparing experimental \bar{p} cross section data and fits we need to specify whether the hyperon contribution is subtracted or not.

For the purpose of astrophysical calculations, of course, our eventual concern is the total \bar{p} cross section including the hyperon contributions. In this section, however, we find it convenient to concentrate first on the prompt \bar{p} production cross section, deferring an analysis of the hyperon contribution to App. B.

1. NA49 experiment

The NA49 experiment reported measurements in a wide kinematic regime. Fig. 1 shows measurements of the p_t -weighted cross section, presented as ratio between NA49 data and the Tan&Ng's formulae in given x_F bins¹. We use data from [20], [21] and [22] for π^+ , K^\pm and \bar{p} respectively. For each point, statistical and systematic errors are both at the level of 10%.

As we discussed, the most relevant kinematical region to determine CR flux is $x_F = 0.1-0.4$. In this region, Fig. 1 shows that apart from an overall factor the fitting functions of Tan&Ng are consistent with the NA49 results for all final states with the possible exception of K^- (the latter being quantitatively irrelevant for the secondary e^+ calculation). Motivated by this result, we introduce a scaling factor $\xi_H(\sqrt{s})$ for each hadron $H = \pi^+, K^\pm, \bar{p}$, and parametrize the cross section as

$$E \frac{d^3\sigma_H}{dp^3} = E \frac{d^3\sigma_H}{dp^3} \Big|_{\text{Tan\&Ng}} \times \xi_H(\sqrt{s}). \quad (6)$$

We take $\xi_{\pi^+} = \xi_{K^\pm} = 0.9$ and $\xi_{\bar{p}} = 0.8$ at $\sqrt{s} = 17.2$ GeV.

Note that the prompt \bar{p} cross section from NA49 is off by $\sim 20\%$ from the inclusive Tan&Ng fit: this is not a discrepancy, but is mainly due to the hyperon contribution

¹ NA49 data are provided in terms of the Feynman parameter $x_F = 2p_L^*/\sqrt{s}$ (where p_L^* is the hadron longitudinal momentum in the CM frame) instead of x_R , so we consider the p_t -weighted cross section at fixed x_F .

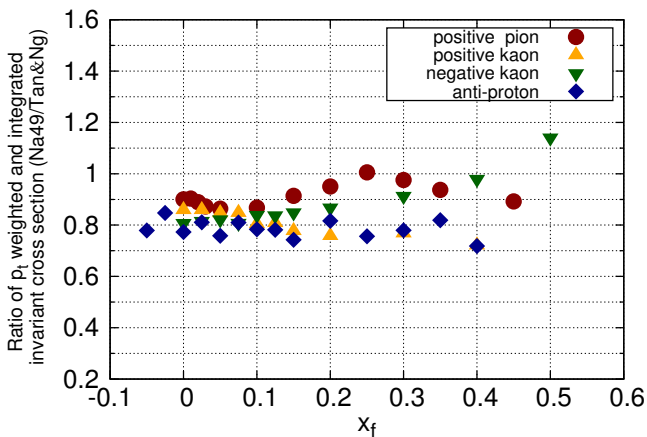


FIG. 1: p_t -weighted cross section for π^+ , K^\pm and \bar{p} , presented as ratio between NA49 data and Tan&Ng [11] inclusive cross section formulae, in given x_F bins. Note that the Tan&Ng formulae include contributions from unstable intermediate states, such as the hyperon contribution $\bar{\Lambda} \rightarrow \bar{p}\pi^+$ to \bar{p} production, that is subtracted in the NA49 \bar{p} data. We explain how to correct for this effect in the text.

present in the Tan&Ng fit while being subtracted from NA49 data. Accounting for this correction we find, in fact, that the inclusive Tan&Ng fit is in good agreement with that deduced from NA49 data.

2. High energy experiments

Next, we analyse the high energy data to determine the behaviour of ξ_H at large \sqrt{s} . The scaling factors ξ_H are calibrated to reproduce the p_t -weighted cross section of Eq. (3) evaluated on the high energy experimental data. Fig. 2 shows the \sqrt{s} dependence of ratios of p_t -weighted cross sections for π^+ , K^\pm and \bar{p} between high energy data and the Tan&Ng [11] formulae. Solid lines indicate the correction functions Eqs. (7-9). We use data from PHENIX [19] at $\sqrt{s} = 62.4, 200$ GeV, CMS [18] at $\sqrt{s} = 900, 2760, 7000$ GeV and ALICE [15, 17] at $\sqrt{s} = 900, 7000$ GeV.

We calculate the p_t -weighted cross section using the p_t range provided by the experiments. Since CMS and ALICE gives a production yield, we use a fitting function of inelastic total scattering rate in [5] to obtain the cross section. In addition, to obtain inelastic yield for CMS, we multiply an empirical factor 0.78 (see [18]). For ALICE data, we use dN/dy estimated in [15, 17]. Statistical and systematic errors are roughly 10% for all experiments apart from the PHENIX \bar{p} data, to which we refer in more detail below.

The orange points in Fig. 2 summarise the collection of experimental data used by the Tan&Ng original analysis [11]. These early measurements cover a wide range of phase space and energy, corresponding to $\sqrt{s} \simeq 10 - 60$ GeV. Detailed comparison shows that the Tan&Ng fits

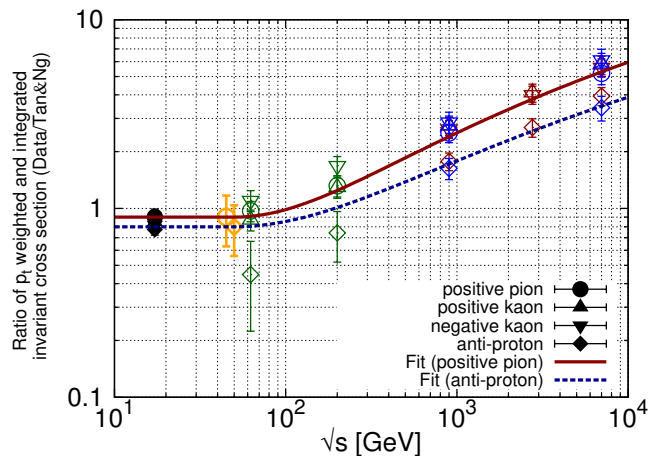


FIG. 2: \sqrt{s} dependence of ratios of p_t -weighted cross sections for π^+ , K^\pm and \bar{p} between high energy experiments and Tan&Ng [11]. Solid lines indicate the correction functions ξ_H . Black, orange, green, blue and red points correspond to NA49, PHENIX, ALICE and CMS data respectively, with estimated systematic uncertainties. The yellow points represent data sets used in Tan&Ng fitting paper [11].

are consistent with these data to within $\sim \pm 30\%$, comparable to the internal variation between the results of individual analyses in this data set, and we assign this uncertainty to the orange points.

We find that the correction functions

$$\xi_{\pi^+}(\sqrt{s}) = \begin{cases} 0.9 & (\sqrt{s} < 50 \text{ GeV}) \\ 0.9 + 0.18[\log(\sqrt{s}/50 \text{ GeV})]^2 & (\sqrt{s} \geq 50 \text{ GeV}) \end{cases}, \quad (7)$$

$$\xi_{\bar{p}}(\sqrt{s}) = \begin{cases} 0.8 & (\sqrt{s} < 50 \text{ GeV}) \\ 0.8 + 0.11[\log(\sqrt{s}/50 \text{ GeV})]^2 & (\sqrt{s} \geq 50 \text{ GeV}) \end{cases}, \quad (8)$$

$$\xi_{K^\pm}(\sqrt{s}) = \xi_{\pi^+}(\sqrt{s}), \quad (9)$$

reproduce the experimentally determined p_t -weighted cross sections in the range $\sqrt{s} \leq 7$ TeV.

Several comments are in order. First, the PHENIX \bar{p} data [19] in Fig. 2 exhibit larger uncertainty compared to most of the other measurements, and the central values are indeed correspondingly off by $\sim 50\%$, 30% for $\sqrt{s}=62.4$ and 200 GeV from the fit. To estimate the p_t -weighted \bar{p} cross section from [19] we start with the data without feed-down correction, as the feed-down corrected cross section is found to be lower by a factor of a few in low p_t bins, which appears broadly inconsistent with the remaining data set. To estimate the feed-down corrected result, we subtract 30% off the inclusive result, as suggested by our analysis in App. B. The \bar{p} systematic uncertainties quoted in [19] are sizeable, notably in the lower p_t region, due to the feed-down correction and take maximally $\sim 50\%$, 30% for $\sqrt{s}=62.4$ and 200 GeV. In Fig. 2, we assign these conservative uncertainty estimates of 50% and 30% to these data. In addition to the feed-down uncertainty, the p_t range covered by the \bar{p}

cross section data in [19] is limited, starting from $p_t = 0.6$ GeV. This means that the p_t -weighted cross section estimate derived from these data is based on a kinematically sub-dominant region for astrophysical purposes.

Second, we comment on the K_S contribution to the π cross section. In the analysis of Fig. 2, we assume that the π cross sections reported by the experiments are prompt and do not include π from K_S decay. The NA49 and CMS experiments explicitly state that π from K_S decay are discriminated in their analyses. On the other hand, the treatment in the PHENIX and ALICE experiment is unclear. This makes 5 % ambiguity of the points from PHENIX and ALICE experiments in Fig. 2. In practice, this ambiguity is not quantitatively important for the determination of fitting formula.

Finally, we comment on the x_R dependence in the high \sqrt{s} regime. The high energy experimental data from [15, 17–19] is only specified at mid-rapidity ($x_R \simeq 0$). This means that our fit could fail to reproduce the x_R dependence in the high \sqrt{s} regime. Fixing this caveat would require cross section data at non-zero x_R (forward region) in the high \sqrt{s} regime.

C. Comparison to previous work

In Fig. 3 we show the secondary source terms for \bar{p} and π^+ , assuming pp production from a power-law primary proton flux $J_p \propto E_p^{-3}$, comparing our results to the fitting formulae of [5] and Tan&Ng. For \bar{p} production, we now include the contributions from both hyperon decay and decay in flight of \bar{n} , using the procedure defined in App. B. The Black line shows the \bar{p} source term ratio between that obtained using the fit of Ref. [5] (denoted “Winkler”) and ours. We find agreement to the 10% level. The blue dotted (red dashed) line shows the \bar{p} (π^+) source term ratio between Tan&Ng [11] and ours. The deviation from radial scaling, assumed in Tan&Ng, is clear at high energy.

III. THE e^+/\bar{p} FLUX RATIO

Ref. [24] pointed out that the production rate ratio $Q_{e^+}/Q_{\bar{p}}$ provides a model-independent upper bound to the flux ratio of high-energy secondary CR e^+ and \bar{p} :

$$\frac{J_{e^+}(\mathcal{R})}{J_{\bar{p}}(\mathcal{R})} < \frac{Q_{e^+}(\mathcal{R})}{Q_{\bar{p}}(\mathcal{R})}, \quad (10)$$

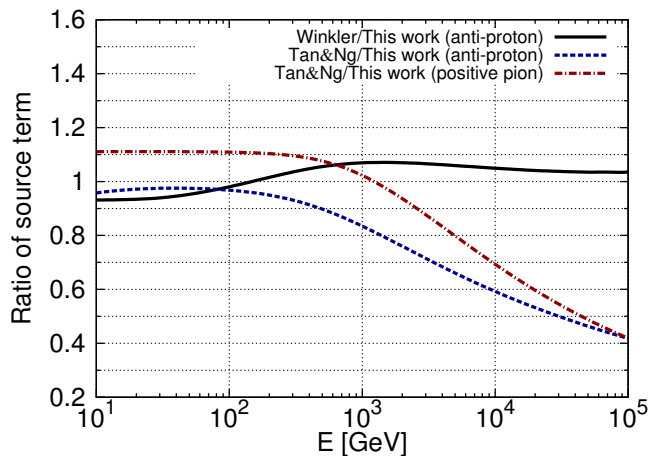


FIG. 3: \sqrt{s} dependence of The ratios of source term assuming $J_p \propto E_p^{-3}$. The Black line shows the \bar{p} source term ratio between that obtained using the fit of Ref. [5] (denoted “Winkler”) and ours. The blue dotted (red dashed) line shows the \bar{p} (π^+) source term ratio between Tan&Ng [11] and ours.

where the source terms for secondary \bar{p} and e^+ produced in pp collisions are²:

$$Q_{\bar{p}}(E_{\bar{p}}) = 2 \int_{E_{\bar{p}}}^{\infty} dE_p 4\pi J_p(E_p) \frac{d\sigma_{pp \rightarrow \bar{p}}}{dE_{\bar{p}}}(E_p; E_{\bar{p}}), \quad (11)$$

$$Q_{e^+}(E_{e^+}) = \int_{E_{e^+}}^{\infty} dE_p 4\pi J_p(E_p) \frac{d\sigma_{pp \rightarrow e^+}}{dE_{e^+}}(E_p; E_{e^+}). \quad (12)$$

This upper bound only depends on the inclusive production cross sections and the shape of proton cosmic ray flux J_p .

We are now in position to extend the calculation of $Q_{e^+}(\mathcal{R})/Q_{\bar{p}}(\mathcal{R})$ to high energy, and compare with the latest CR data. In Fig. 4 we show the upper bound predicted for different assumptions on the primary proton flux in the spallation region. The e^+/\bar{p} flux ratio measured by AMS-02 is consistent with the upper bound and saturates it at high energy (for proton flux coinciding with the locally measured proton flux).

Recent calculations of the high-energy secondary CR \bar{p} flux [23, 25], using up to date \bar{p} production cross section consistent with our results here and calibrated to agree with AMS-02 B/C data, are consistent with the CR \bar{p} flux measured by AMS-02. These results are reproduced in App. C. The significance, in connection with Fig. 4, is that the observed flux of CR e^+ at $\mathcal{R} > 100$ GV coincides with the expected flux of secondary e^+ , that would be expected if radiative energy loss became unimportant in

² Note that (i) the factor 2 in $Q_{\bar{p}}$ comes from decay in flight of \bar{n} , and (ii) the normalization in our definition for $Q_{e^+, \bar{p}}$ here is somewhat different than in, e.g., Refs. [23–25]. This is for ease of presentation and is of no consequence for the source ratio.

Acknowledgements

This research is supported by grant 1937/12 from the I-CORE program of the Planning and Budgeting Committee and the Israel Science Foundation and by grant 1507/16 from the Israel Science Foundation. The work of MT is supported by the JSPS Research Fellowship for Young Scientists. KB is incumbent of the Dewey David Stone and Harry Levine career development chair.

Appendix A: Neutral kaon contributions

In this section we calculate the final state e^+ contribution coming from the decay of K_L^0 mesons. This contribution has been neglected in the literature, although the corresponding cross section is comparable to that for charged kaons which was previously taken into account. K_L^0 mesons are long-lived ($c\tau_{K_L^0} \simeq 15$ m) in the collider set-up, so that π^+ from K_L^0 decay are not included in the fitting formula of the inclusive π^+ cross section. In addition, the K_L^0 semi-leptonic decay contributes directly to e^+ and $\mu^+(\rightarrow e^+)$ production.

We consider the following decay channels [29]:

$$\text{Br}(K_L^0 \rightarrow \pi^\pm e^\mp \nu_e) = 40.55 \%, \quad (\text{A1})$$

$$\text{Br}(K_L^0 \rightarrow \pi^\pm \mu^\mp \nu_e) = 27.04 \%, \quad (\text{A2})$$

$$\text{Br}(K_L^0 \rightarrow \pi^+ \pi^- \pi^0) = 12.54 \%. \quad (\text{A3})$$

We approximate and simplify the kinematics of K_L^0 three-body decays, assigning each of the decay products an energy of $m_K/3$ in the K_L^0 rest frame and ignoring muon polarisation. We approximate the K_L^0 production cross section to match that of K^+ . The e^+ spectrum from boosted μ^+ is given in Ref. [30] and the e^+ spectrum from boosted π^+ is given in Ref. [31].

The kaon contribution to astrophysical secondary e^+ production is highlighted in Fig. 5. The K_L^0 contribution amounts roughly to 5% of the total e^+ source.

Appendix B: Antiproton cross section including anti-hyperon contributions

In this section we analyse the hyperon contribution to the inclusive \bar{p} production cross section. We denote the Lorentz-invariant differential cross section as f ;

$$f_{\#}^\bullet \equiv E \frac{d^3 \sigma_{\#}^\bullet}{dp^3}. \quad (\text{B1})$$

The astrophysically relevant inclusive $f_{\bar{p}}^{\text{tot}}$, which includes effects from \bar{n} and hyperon decays, can be decomposed in the following way:

$$f_{\bar{p}}^{\text{tot}} = f_{\bar{p}} + f_{\bar{n}}, \quad (\text{B2})$$

$$f_{\bar{p}} = f_{\bar{p}}^0 + f_{\bar{p}}^\Lambda + f_{\bar{p}}^\Sigma, \quad (\text{B3})$$

$$f_{\bar{n}} = f_{\bar{n}}^0 + f_{\bar{n}}^\Lambda + f_{\bar{n}}^\Sigma, \quad (\text{B4})$$

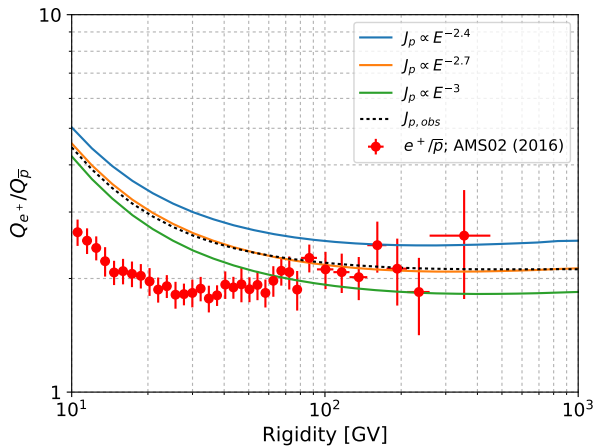


FIG. 4: The ratio of $Q_{e^+}/Q_{\bar{p}}$. The dashed line is calculated by using the observed proton flux. Blue, orange, and green solid lines are calculated by assuming $J_p \propto E^{-2.4}$, $E^{-2.7}$, E^{-3} , respectively. The observational data e^+/\bar{p} is taken from Ref. [3].

the propagation at these energies. Achieving such low level of energy loss would require that the characteristic secondary CR propagation time drops below a few Myr at $\mathcal{R} > 100$ GV.

A comparison of the source ratio $Q_{e^+}/Q_{\bar{p}}$ to the observed e^+/\bar{p} flux ratio was also presented in Ref. [26], which found results for $Q_{e^+}/Q_{\bar{p}}$ smaller than our value by $\sim 30\%$ in the energy range 10 – 1000 GeV. This led Ref. [26] to argue that e^+ energy losses may be negligible at all energies (rather than only at $E \gtrsim 100$ GeV, as suggested by our Fig. 4). We have not been able to reproduce the origin of this discrepancy.

IV. CONCLUSIONS

We presented an analysis of inclusive \bar{p} , π , and K production in pp collisions. Our main goal was to implement recent experimental data for meson production, in particular the effect of radial scaling violation manifest at LHC energies and recent detailed kinematical data from the NA49 experiment at intermediate energy, in semi-analytic fits used for the calculation of the astrophysical secondary production of e^+ . We provide fitting formulae that, combined with earlier results from Tan&Ng [11], allow to compute the astrophysical production of e^+ and \bar{p} up to the multi-TeV range with an estimated uncertainty of $\sim 20\%$.

The e^+/\bar{p} flux ratio reported by AMS-02 is found to coincide with the secondary source production rate ratio $Q_{e^+}/Q_{\bar{p}}$ at high-energy $E > 100$ GeV. This coincidence may be considered as a hint for a secondary origin for CR e^+ and \bar{p} , as it would be a fine-tuned accident in models that advocate new primary sources for either antimatter CR species.

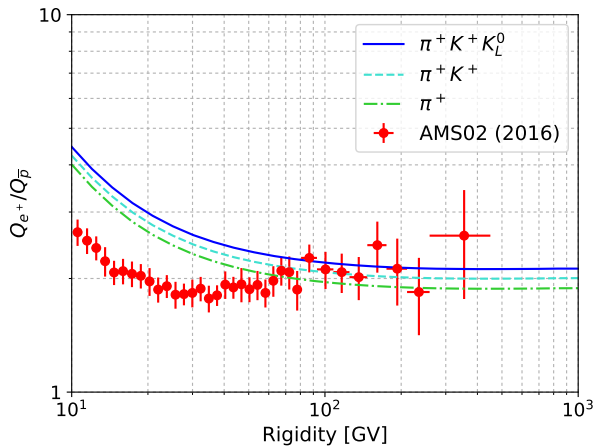


FIG. 5: Same as in Fig. 4, but highlighting the kaon contribution to the source term of secondary e^+ . The proton spectrum is assumed to follow $J_p \propto E^{-2.7}$.

where f^0 indicates the prompt contribution and $f^{\bar{\Lambda}, \bar{\Sigma}}$ denote contribution from the hyperon decay. Neglecting isospin violation, we assume $f_{\bar{p}}^0 = f_{\bar{n}}^0$. To set a rough scale for the effect we're after here, the analysis in Sec. II shows $f_{\bar{p}}^0 \simeq 0.8 f_{\bar{p}}^{\text{Tan\&Ng}}$ at low \sqrt{s} , where $f_{\bar{p}}^{\text{Tan\&Ng}}$ includes the hyperon decay contribution. (See Eq. (8) and Fig. 2.)

1. Anti-hyperon production cross section at the NA49 experiment

NA49 [20] results indicate that the kinematical distribution of anti-hyperons produced in pp collisions is somewhat different from that of anti-nucleons³. We introduce x_R -dependent functions $g_{\bar{B}}(x_R)$ with $\bar{B} = \bar{\Lambda}, \bar{\Sigma}^\pm$, and parametrize the hyperon contributions as

$$f_{\bar{p}}^{\bar{\Lambda}} = f_{\bar{p}}^{\text{Tan\&Ng}} g_{\bar{\Lambda}}(x_R) \text{Br}(\Lambda \rightarrow pX), \quad (\text{B5})$$

$$f_{\bar{n}}^{\bar{\Lambda}} = f_{\bar{p}}^{\text{Tan\&Ng}} g_{\bar{\Lambda}}(x_R) \text{Br}(\Lambda \rightarrow nX), \quad (\text{B6})$$

$$f_{\bar{p}}^{\bar{\Sigma}^-} = f_{\bar{p}}^{\text{Tan\&Ng}} g_{\bar{\Sigma}^-}(x_R) \text{Br}(\Sigma^+ \rightarrow pX), \quad (\text{B7})$$

$$f_{\bar{n}}^{\bar{\Sigma}^-} = f_{\bar{p}}^{\text{Tan\&Ng}} g_{\bar{\Sigma}^-}(x_R) \text{Br}(\Sigma^+ \rightarrow nX) \\ + f_{\bar{p}}^{\text{Tan\&Ng}} g_{\bar{\Sigma}^+}(x_R) \text{Br}(\Sigma^- \rightarrow nX). \quad (\text{B8})$$

The branching fractions for hyperon decays are $\text{Br}(\Lambda \rightarrow pX) \simeq 0.64$, $\text{Br}(\Lambda \rightarrow nX) \simeq 0.36$, $\text{Br}(\Sigma^+ \rightarrow pX) \simeq 0.52$, $\text{Br}(\Sigma^+ \rightarrow nX) \simeq 0.48$ and $\text{Br}(\Sigma^- \rightarrow nX) \simeq 1$ [32]. Summing up, we obtain

$$f_{\bar{p}}^{\text{tot}} \simeq f_{\bar{p}}^{\text{Tan}} \times [1.6 + g_{\bar{\Lambda}} + g_{\bar{\Sigma}^-} + g_{\bar{\Sigma}^+}]. \quad (\text{B9})$$

³ This conclusion is in some tension with the parallel discussion presented in [5], which will lead us to slightly different results.

We neglect momentum difference between parent and daughter particle since their mass difference is $\lesssim 20\%$.

Let us determine $g_{\bar{B}}(x_R)$. NA49 analysis [20] (see Fig. 22 there) offers the differential multiplicity dn/dx_F for Λ , $\bar{\Lambda}$, Σ^+ , Σ^- , defined as

$$\frac{dn_{\bullet}(x_F)}{dx_F} = \frac{\pi}{\sigma_{\text{inel}}} \frac{\sqrt{s}}{2} \int dp_t^2 \frac{f_{\bullet}}{E}. \quad (\text{B10})$$

Uncertainties of dn/dx_F are not presented, but a typical error estimate of $\sim 20\%$ can be inferred from the analysis in [5].

Although the definition of $x_R (= E^*/E_{\text{max}}^*)$ and $x_F (= 2p_L^*/\sqrt{s})$ are different, their difference is of the order of p_L^2/s or m_p^2/s . Thus, $g_{\bar{B}}(x_R)$ can be determined from the observation of dn/dx_F . As discussed in section II, $0.1 \lesssim x_R \lesssim 0.4$ is the important kinematical region to determine secondary cosmic ray production. In this region, the p_t dependence on E becomes weak and dn/dx_F is determined by p_t weighted averaged cross-section. In this respect, we find that dn/dx_F is a directly relevant quantity for secondary cosmic ray production. Then, it is reasonable to estimate

$$g_{\bar{B}}(x_R) = \left[\left(\frac{dn_{\bar{B}}}{dx_F} \right) / \left(\frac{dn_{\bar{p}}}{dx_F} \Big|_{\text{Tan\&Ng}} \right) \right] \Big|_{x_F=x_R}, \quad (\text{B11})$$

with $\bar{B} = \Lambda, \bar{\Lambda}, \Sigma^+, \Sigma^-$ or \bar{p} .

Following Ref. [22] we assume the relation

$$\frac{dn_{\bar{\Sigma}^-}}{dx_F} \simeq 0.8 \times \frac{dn_{\bar{\Lambda}}/dx_F}{dn_{\Lambda}/dx_F} \frac{dn_{\Sigma^+}}{dx_F}. \quad (\text{B12})$$

Then, we expect

$$g_{\bar{\Sigma}^-} \simeq 0.8 \times \frac{dn_{\bar{\Lambda}}/dx_F}{dn_{\Lambda}/dx_F} g_{\Sigma^+}. \quad (\text{B13})$$

We assume a similar relation for $\bar{\Sigma}^+$:

$$g_{\bar{\Sigma}^+} \simeq 0.8 \times \frac{dn_{\bar{\Lambda}}/dx_F}{dn_{\Lambda}/dx_F} g_{\Sigma^-}. \quad (\text{B14})$$

To obtain $g_{\bar{B}}$ (with $B = \Lambda, \Sigma^\pm$), we fit the x_F dependence shown in the NA49 analysis by the following form:

$$g_{\bar{B}} = a(1 - x_R)^n. \quad (\text{B15})$$

We found $(a, n) = (0.13, -3)$, $(0.038, -3)$, $(0.028, -2)$ well fit $\bar{\Lambda}$, $\bar{\Sigma}^-$, $\bar{\Sigma}^+$ respectively.

Fig. 6 shows the x_F dependent $\bar{B} \equiv dn_{\bar{B}}/dx_F$. Solid and dashed lines correspond to NA49 values and our fitting function, respectively.

2. Multiplicity of anti-hyperons at large \sqrt{s}

For relatively small $\sqrt{s} < 50$ GeV, we expect that Eq. (B9) holds with weak \sqrt{s} dependence. This is because, empirically, radial scaling applies at small \sqrt{s} .

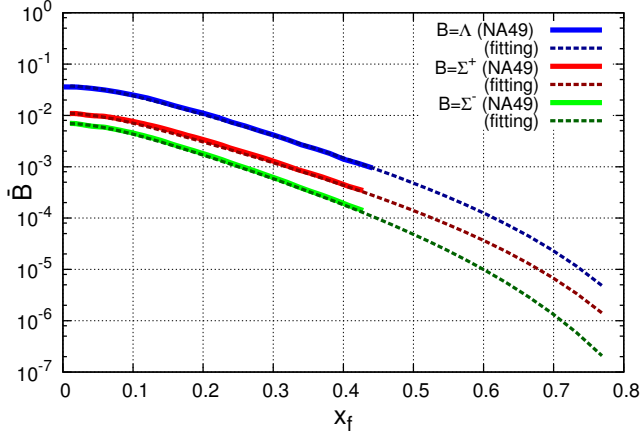


FIG. 6: x_F dependent $\bar{B} \equiv dn_{\bar{B}}/dx_F$. The solid lines and dashed ones correspond to NA49 values and our fitting function, respectively.

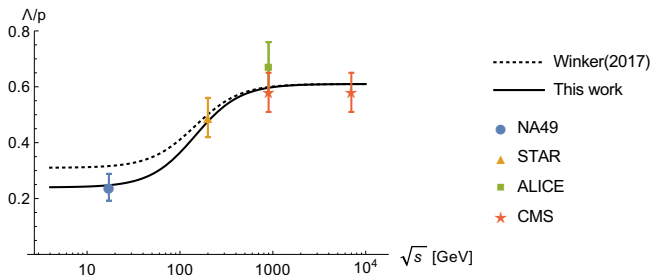


FIG. 7: $\bar{\Lambda}/\bar{p}$ ratio in proton-proton collision at mid-rapidity.

However, when we consider large $\sqrt{s} > 50$ GeV, we have to consider the violation of radial scaling.

Ref. [5] showed that the ratio between the multiplicity of anti-hyperons and \bar{p} is not constant as function of \sqrt{s} . Following [5], we introduce \sqrt{s} dependence as an overall factor to the hyperon contributions,

$$f_{\bar{p}}^{\text{tot}} \simeq f_{\bar{p}}^{\text{Tan}} \times [1.6 \times \xi(\sqrt{s}) + (g_{\bar{\Lambda}} + g_{\bar{\Sigma}^-} + g_{\bar{\Sigma}^+}) \times \kappa(\sqrt{s})]. \quad (\text{B16})$$

Here $\kappa(\sqrt{s})$ satisfies $\lim_{s \rightarrow 0} \kappa(\sqrt{s}) = 1$, and deviates from unity at large \sqrt{s} .

We define the ratio between the multiplicity of $\bar{\Lambda}$ and \bar{p} at midrapidity:

$$\frac{\bar{\Lambda}}{\bar{p}} = \frac{dn_{\bar{\Lambda}}/dx_F}{dn_{\bar{p}}/dx_F} \Big|_{x_F=0}. \quad (\text{B17})$$

For simplicity, we assume that $\bar{\Lambda}$, $\bar{\Sigma}^{\pm}$ have the same scaling law for their multiplicity. By using this assumption, we take $\kappa(\sqrt{s})$ as

$$\kappa(\sqrt{s}) = \frac{(\bar{\Lambda}/\bar{p})(\sqrt{s})}{(\bar{\Lambda}/\bar{p})(0)}. \quad (\text{B18})$$

Finally, we analyse the ratio $\bar{\Lambda}/\bar{p}$ using data from STAR [33, 34], ALICE [15, 35], and CMS [18, 36] which provided multiplicity ratios at mid-rapidity. NA49 also provided differential multiplicity at the mid-rapidity; we assume an uncertainty of 20% from the uncertainty in the feed-down correction. This gives us $\bar{\Lambda}/\bar{p} = 0.24 \pm 0.05$ at $\sqrt{s} = 17.2$ GeV from NA49 experiment.

Fig. 7 shows our result. For comparison, we also show $\bar{\Lambda}/\bar{p}$ as found in [5]. Our results can be fitted by the following formula:

$$\frac{\bar{\Lambda}}{\bar{p}} = 0.24 + \frac{0.37}{1 + ((146 \text{ GeV})^2/s)^{0.9}}. \quad (\text{B19})$$

Appendix C: Secondary \bar{p}

Fig. 8 shows the secondary \bar{p} cosmic ray flux predicted by our cross section formula, calculated under the assumption that the mean target column density traversed by CR protons; He; nuclei such as B, C, and O; and \bar{p} is the same as function of magnetic rigidity [24]. The column density used in the calculation is extracted from B/C data using fragmentation cross sections as specified in [23].

The simple estimate in Fig. 8 is consistent the AMS-02 \bar{p} data [3]. The calculation is sensitive to a number of systematic uncertainties. The blue region shows the uncertainty of the solar modulation parameter $\phi = (0.2 - 0.8)$ GV. The grey region shows the result of varying the spectral index of proton CR above 300 GV. We vary γ_p in the range of 2.6–2.8 where $J_p \propto E_p^{-\gamma_p}$: this should represent the possibility that the CR proton spectrum in the regions dominating secondary \bar{p} production may not be identical to the locally measured spectrum. The solid green lines show the result of varying the C \rightarrow B fragmentation cross section by $\pm 20\%$. Finally, the dashed dark lines represent \bar{p} production cross section uncertainty of $\pm 20\%$.

[1] **AMS** Collaboration, L. Accardo *et al.*, “High Statistics Measurement of the Positron Fraction in Primary Cosmic Rays of 0.5-500 GeV with the Alpha Magnetic Spectrometer on the International Space Station,”

Phys. Rev. Lett. **113** (2014) 121101.

[2] **AMS** Collaboration, M. Aguilar *et al.*, “Electron and Positron Fluxes in Primary Cosmic Rays Measured with the Alpha Magnetic Spectrometer on the International

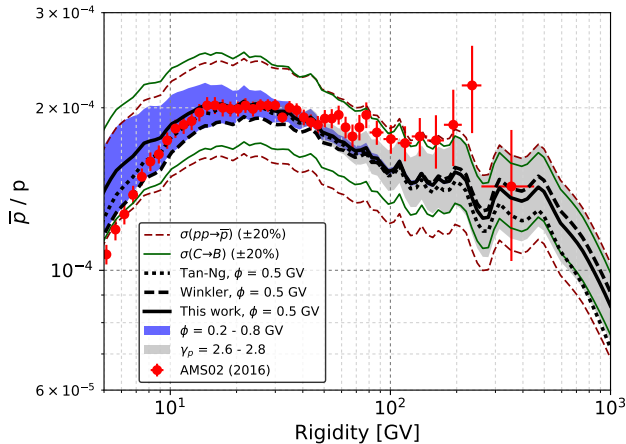


FIG. 8: Cosmic ray \bar{p} flux for several cross section formulae. In all cases, we use the mean traversed target column density extracted from B/C data [24] using nuclear fragmentation cross sections as specified in [23]. Solid black line shows the prediction using our fit. Dotted and dashed black lines show to the result when using the fit from Tan&Ng [11] and Winkler [5], respectively. Other bands and lines show various sources of systematic uncertainty; see text for details.

- Space Station,” *Phys. Rev. Lett.* **113** (2014) 121102.
- [3] **AMS** Collaboration, M. Aguilar *et al.*, “Antiproton Flux, Antiproton-to-Proton Flux Ratio, and Properties of Elementary Particle Fluxes in Primary Cosmic Rays Measured with the Alpha Magnetic Spectrometer on the International Space Station,” *Phys. Rev. Lett.* **117** no. 9, (2016) 091103.
- [4] M. di Mauro, F. Donato, A. Goudelis, and P. D. Serpico, “New evaluation of the antiproton production cross section for cosmic ray studies,” *Phys. Rev.* **D90** no. 8, (2014) 085017, [arXiv:1408.0288 \[hep-ph\]](#).
- [5] M. W. Winkler, “Cosmic Ray Antiprotons at High Energies,” *JCAP* **1702** no. 02, (2017) 048, [arXiv:1701.04866 \[hep-ph\]](#).
- [6] F. Donato, M. Korsmeier, and M. Di Mauro, “Prescriptions on antiproton cross section data for precise theoretical antiproton flux predictions,” [arXiv:1704.03663 \[astro-ph.HE\]](#).
- [7] I. V. Moskalenko and A. W. Strong, “Production and propagation of cosmic ray positrons and electrons,” *Astrophys. J.* **493** (1998) 694–707, [arXiv:astro-ph/9710124 \[astro-ph\]](#).
- [8] T. Delahaye, F. Donato, N. Fornengo, J. Lavalle, R. Lineros, P. Salati, and R. Taillet, “Galactic secondary positron flux at the Earth,” *Astron. Astrophys.* **501** (2009) 821–833, [arXiv:0809.5268 \[astro-ph\]](#).
- [9] R. Kappl and A. Reinert, “Secondary Cosmic Positrons in an Inhomogeneous Diffusion Model,” *Phys. Dark Univ.* **16** (2017) 71–80, [arXiv:1609.01300 \[astro-ph.HE\]](#).
- [10] T. Kamae, N. Karlsson, T. Mizuno, T. Abe, and T. Koi, “Parameterization of Gamma, e+/- and Neutrino Spectra Produced by p-p Interaction in Astronomical Environment,” *Astrophys. J.* **647** (2006) 692–708, [arXiv:astro-ph/0605581 \[astro-ph\]](#). [Erratum: *Astrophys. J.* 662,779(2007)].
- [11] L. C. Tan and L. K. Ng, “PARAMETRIZATION OF HADRON INCLUSIVE CROSS-SECTIONS IN P P COLLISIONS EXTENDED TO VERY LOW-ENERGIES,” *J. Phys.* **G9** (1983) 1289–1308.
- [12] R. P. Feynman, “Very high-energy collisions of hadrons,” *Phys. Rev. Lett.* **23** (1969) 1415–1417.
- [13] K. Kinoshita and H. Noda, “Inclusive reactions and urbaryon rearrangement diagrams,” *Prog. Theor. Phys.* **46** (1971) 1639–1641.
- [14] K. Kinoshita and H. Noda, “Increase of single-particle spectra and a new form of scaling. inclusive reactions and urbaryon rearrangement diagrams. v,” *Prog. Theor. Phys.* **49** (1973) 896–913.
- [15] **ALICE** Collaboration, K. Aamodt *et al.*, “Production of pions, kaons and protons in pp collisions at $\sqrt{s} = 900$ GeV with ALICE at the LHC,” *Eur. Phys. J.* **C71** (2011) 1655, [arXiv:1101.4110 \[hep-ex\]](#).
- [16] **ALICE** Collaboration, B. B. Abelev *et al.*, “Production of charged pions, kaons and protons at large transverse momenta in pp and PbPb collisions at $\sqrt{s_{NN}} = 2.76$ TeV,” *Phys. Lett.* **B736** (2014) 196–207, [arXiv:1401.1250 \[nucl-ex\]](#).
- [17] **ALICE** Collaboration, J. Adam *et al.*, “Measurement of pion, kaon and proton production in protonproton collisions at $\sqrt{s} = 7$ TeV,” *Eur. Phys. J.* **C75** no. 5, (2015) 226, [arXiv:1504.00024 \[nucl-ex\]](#).
- [18] **CMS** Collaboration, S. Chatrchyan *et al.*, “Study of the inclusive production of charged pions, kaons, and protons in pp collisions at $\sqrt{s} = 0.9, 2.76,$ and 7 TeV,” *Eur. Phys. J.* **C72** (2012) 2164, [arXiv:1207.4724 \[hep-ex\]](#).
- [19] **PHENIX** Collaboration, A. Adare *et al.*, “Identified charged hadron production in p + p collisions at $\sqrt{s} = 200$ and 62.4 GeV,” *Phys. Rev.* **C83** (2011) 064903, [arXiv:1102.0753 \[nucl-ex\]](#).
- [20] **NA49** Collaboration, C. Alt *et al.*, “Inclusive production of charged pions in p+p collisions at 158-GeV/c beam momentum,” *Eur. Phys. J.* **C45** (2006) 343–381, [arXiv:hep-ex/0510009 \[hep-ex\]](#).
- [21] **NA49** Collaboration, T. Anticic *et al.*, “Inclusive production of charged kaons in p+p collisions at 158 GeV/c beam momentum and a new evaluation of the energy dependence of kaon production up to collider energies,” *Eur. Phys. J.* **C68** (2010) 1–73, [arXiv:1004.1889 \[hep-ex\]](#).
- [22] **NA49** Collaboration, T. Anticic *et al.*, “Inclusive production of protons, anti-protons and neutrons in p+p collisions at 158-GeV/c beam momentum,” *Eur. Phys. J.* **C65** (2010) 9–63, [arXiv:0904.2708 \[hep-ex\]](#).
- [23] K. Blum, K. C. Y. Ng, R. Sato, and M. Takimoto, “Cosmic rays, anti-helium, and an old navy spotlight,” [arXiv:1704.05431 \[astro-ph.HE\]](#).
- [24] B. Katz, K. Blum, and E. Waxman, “What can we really learn from positron flux ‘anomalies’?,” *Mon. Not. Roy. Astron. Soc.* **405** (2010) 1458, [arXiv:0907.1686 \[astro-ph.HE\]](#).
- [25] K. Blum, B. Katz, and E. Waxman, “AMS-02 Results Support the Secondary Origin of Cosmic Ray Positrons,” *Phys. Rev. Lett.* **111** no. 21, (2013) 211101, [arXiv:1305.1324 \[astro-ph.HE\]](#).
- [26] P. Lipari, “Interpretation of the cosmic ray positron and antiproton fluxes,” *Phys. Rev.* **D95** no. 6, (2017)

- 063009, [arXiv:1608.02018](#) [astro-ph.HE].
- [27] L. C. Tan and L. K. Ng, “PARAMETRIZATION OF ANTI-P INVARIANT CROSS-SECTION IN P P COLLISIONS USING A NEW SCALING VARIABLE,” *Phys. Rev.* **D26** (1982) 1179–1182.
- [28] G. D. Badhwar, S. A. Stephens, and R. L. Golden, “Analytic Representation of the Proton Proton and Proton-Nucleus Cross-Sections and Its Application to the Sea Level Spectrum and Charge Ratio of Muons,” *Phys. Rev.* **D15** (1977) 820–831.
- [29] **Particle Data Group** Collaboration, C. Patrignani *et al.*, “Review of Particle Physics,” *Chin. Phys.* **C40** no. 10, (2016) 100001.
- [30] J. H. Scanlon and S. Milford, “Energy spectra of electrons from pi-mu-e decays in interstellar space.,” *The Astrophysical Journal* **141** (1965) 718.
- [31] C. D. Dermer, “Binary collision rates of relativistic thermal plasmas. ii-spectra,” *The Astrophysical Journal* **307** (1986) 47–59.
- [32] **Particle Data Group** Collaboration, C. Patrignani *et al.*, “Review of Particle Physics,” *Chin. Phys.* **C40** no. 10, (2016) 100001.
- [33] **STAR** Collaboration, B. I. Abelev *et al.*, “Strange particle production in p+p collisions at $s^{*}(1/2) = 200\text{-GeV}$,” *Phys. Rev.* **C75** (2007) 064901, [arXiv:nuc1-ex/0607033](#) [nucl-ex].
- [34] **STAR** Collaboration, B. I. Abelev *et al.*, “Systematic Measurements of Identified Particle Spectra in pp, d^+ Au and Au+Au Collisions from STAR,” *Phys. Rev.* **C79** (2009) 034909, [arXiv:0808.2041](#) [nucl-ex].
- [35] **ALICE** Collaboration, K. Aamodt *et al.*, “Strange particle production in proton-proton collisions at $\sqrt{s} = 0.9\text{ TeV}$ with ALICE at the LHC,” *Eur. Phys. J.* **C71** (2011) 1594, [arXiv:1012.3257](#) [hep-ex].
- [36] **CMS** Collaboration, V. Khachatryan *et al.*, “Strange Particle Production in pp Collisions at $\sqrt{s} = 0.9$ and 7 TeV,” *JHEP* **05** (2011) 064, [arXiv:1102.4282](#) [hep-ex].